



RESEARCH ARTICLE | OCTOBER 11 2023

Scheme of acoustic radiation force on general uniform structure

Menyang Gong (宫门阳) ; Yupei Qiao (乔玉配) ; Xin Xu (徐鑫) ; Jiehui Liu (刘杰惠); Aijun He (何爱军); Xiaozhou Liu (刘晓宙)  



Physics of Fluids 35, 107117 (2023)

<https://doi.org/10.1063/5.0170190>



CrossMark

Articles You May Be Interested In

Resonant adhesion structure makes negative acoustic radiation force

Physics of Fluids (May 2023)

Non-diffractive acoustic beams produce negative radiation force in certain regions

AIP Advances (June 2021)

Non-invasive manipulation scheme of spherical particle in viscous fluids in a tube based on acoustic radiation force

J. Acoust. Soc. Am. (February 2023)



APL Quantum
Bridging fundamental quantum research with technological applications

Now Open for Submissions
No Article Processing Charges (APCs) through 2024

Submit Today



Scheme of acoustic radiation force on general uniform structure

Cite as: Phys. Fluids **35**, 107117 (2023); doi: [10.1063/5.0170190](https://doi.org/10.1063/5.0170190)

Submitted: 1 August 2023 · Accepted: 25 September 2023 ·

Published Online: 11 October 2023



View Online



Export Citation



CrossMark

Menyang Gong (宫门阳),¹ Yupei Qiao (乔玉配),² Xin Xu (徐鑫),¹ Jiehui Liu (刘杰惠),¹ Aijun He (何爱军),³ and Xiaozhou Liu (刘晓宙)^{1,4,a)}

AFFILIATIONS

¹Key Laboratory of Modern Acoustics, Institute of Acoustics and School of Physics, Collaborative Innovation Center of Advanced Microstructures, Nanjing University, Nanjing 210093, China

²School of Physics and Electronic Science, Guizhou Normal University, Guiyang 550001, China

³School of Electronic Science and Engineering, Nanjing University, Nanjing 210023, China

⁴State Key Laboratory of Acoustics, Institute of Acoustics, Chinese Academy of Sciences, Beijing 100190, China

^{a)} Author to whom correspondence should be addressed: xzliu@nju.edu.cn

ABSTRACT

Acoustic manipulation based on acoustic radiation force (ARF) is an important structure manipulation method, which has a wide application prospect in particle manipulation. The calculation of ARF received by regular particles has been extensively studied. In this paper, the scheme of ARF acting on general structure is proposed. The analytical relationship between the ARF and the velocity potential distribution of the scattering on a specified envelope surface is established directly. The irregular surface integration is extended to a custom surface, which is easy to be processed. The results of the analytical solution and the finite element simulation are given to verify its simplicity and accuracy. This solution has a significant improvement compared with the traditional calculation methods based on definitions, especially avoiding the integration upon complex surfaces. The proposal of this complete scheme makes it possible to calculate the analytical ARF acting on structure with any surface description and lays a complete theoretical foundation for the wide application of ARF in structure and particle manipulation.

Published under an exclusive license by AIP Publishing. <https://doi.org/10.1063/5.0170190>

I. INTRODUCTION

Acoustic radiation force (ARF) is an important nonlinear effect of acoustic waves. Acoustic manipulation tools such as “acoustic tweezers” based on it have an important application prospect in the fields of medicine and materials science. The process of ARF is essentially to impart momentum to the structure through the field, which is also an important method of precise energy transmission in fluid. After the “optical tweezers” proposed by A. Ashkin won the Nobel Prize,¹ the “acoustic tweezers” proposed by J. R. Wu to make up for their shortcomings have gradually become a research hotspot.² Acoustic manipulation is mainly achieved by two methods: one is to construct a potential well through standing wave field to capture and suspend particles; the other is the nonlinear ARF effect of single beam acting on particles to achieve the thrust and pull of particles.^{3–8} To some extent, the acoustic control of single beam is better than that of standing wave field. Without the limitation of small scale ventral wave node, single beam can achieve continuous acoustic control in large space. In practical particle manipulation, sound sources cannot be added in multiple

directions relative to particles in many cases, making single beam implementation the only feasible scheme. Hence, it is quiet urgent to propose a scheme to solve the ARF received by various shapes of structures in the sound field. The ARFs of plane wave, Gaussian wave, and Bessel wave on the near field of regular particles, such as spherical and cylindrical particles, have been widely studied.^{9–31} ARFs on spherical particles with common boundaries also have been studied.^{32,33} Recently, far-field ARF scheme based on X wave has been proposed.³⁴ The possibility of negative ARFs based on non-diffracted waves is verified, which has greatly expanded the application prospects of ARF.³⁵

Traditional methods for calculating ARF mostly use Kirchhoff integration. This integration process is quiet cumbersome and complicated in calculating the structure described by complex surface, and it is difficult to apply this integration to the treatment of scattering structures with non-rigid boundaries. The practical method to compute the ARF on arbitrary shapes uses the conservation of momentum, which can transfer the integration of the acoustic radiation stress tensor from the particle surface to a far-field enclosed spherical surface. This idea

was first implemented for 3D ARF by Silva and Mitri in 2012,³⁶ then by Baresch *et al.* in 2013,¹¹ and by Sapozhnikov and Bailey in 2013.²¹ The three sets of formulas of the 3D ARF are proved to be equivalent by Gong and Baudoin in 2021 with explicit reasons.³⁷ In addition, the T-matrix method is introduced to compute the 3D ARF, which has been proved to be a quite efficient and useful scheme for axisymmetric objects.³⁸ The principle of the proposed scheme in this paper is based on the integral expansion of the transfer matrix. This method circumvents the cumbersome calculation process of Kirchhoff integration for each point of sound pressure in the conventional method. Moreover, the analytical extension method based on the transmission matrix is extended to the structure of non-rigid media. Since the proposed method only focuses on the transmission matrix of the scattered radiation stress tensor, if the structure has a complex shape inside, it can also be treated as a black box, which has specific transfer matrix.

II. THEORETICAL ANALYSIS BASED ON INTEGRAL EXPANSION

For spherical or cylindrical particles with regular structure, the surface can be directly described by analytical mathematical expressions, which is easy to calculate the sound pressure distribution on the surface. However, for the structure with complex surface descriptions, it is difficult in direct calculation. In order to solve this problem, a simple and reliable way to calculate or estimate the transfer matrix of the surface directly is by surface analysis. The transfer matrix method is first introduced by Waterman³⁹ and has been proved as an effective tool to calculate the scattering field. The structure under study is placed in an ideal fluid, and the sound beam is injected from one side. Due to conservation of momentum, the radiation stress tensor in environmental medium (ideal fluid) satisfies the following equation:

$$\nabla \cdot \langle S_T \rangle = 0. \quad (1)$$

According to Gaussian theorem, the integral area of the integral calculation of the radiation pressure flux can be transformed from the structure surface to any envelope surface that contains the structure inside (shown in Fig. 1). So the expression of ARF vs scattering velocity potential can be expressed as follows:³⁸

$$\mathbf{F} = \frac{1}{2} \rho_0 k^2 \iint_{S'} \text{Re} \left[\left(\frac{i}{k} \frac{\partial \Phi_i}{\partial r} - \Phi_i \right) \Phi_s^* - \Phi_s \Phi_s^* \right] \mathbf{n} dS, \quad (2)$$

where, ρ_0 is the density of the surrounding medium. S' is any envelope surface that contains the structure inside. To facilitate calculation, the

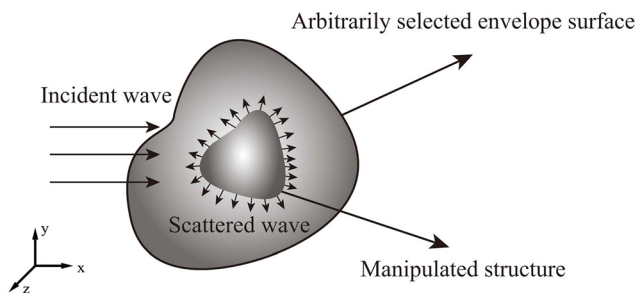


FIG. 1. Schematic diagram of the transformation of the controlled structure surface into an arbitrary envelope surface containing the structure.

envelope surface is usually spherical. Φ_i is the incident wave velocity potential. Φ_s is the scattered wave velocity potential. k is the wave number. Re is the operation of taking the real part. $*$ is the conjugate of the complex parameter. Since the velocity potential of the incident sound wave is known, only the distribution of the scattering velocity potential on the envelope needs to be calculated. Based on Eq. (2), it can be seen that to calculate the ARF received by the structure does not need to calculate the sound scattering of the whole area, only the scattering sound pressure on the specific envelope surface needs to be calculated. The velocity potential of the incident and scattered fields can be written as follows in spherical coordinates:

$$\begin{aligned} \Phi_i &= \sum_{nm} a_{nm} j_n(kr) Y_{nm}(\theta, \phi), \\ \Phi_s &= \sum_{nm} s_{nm} h_n^{(1)}(kr) Y_{nm}(\theta, \phi), \\ Y_{nm}(\theta, \phi) &= P_{nm}(\cos \theta) e^{im\phi}, \end{aligned} \quad (3)$$

where, Y_{nm} is the spherical harmonic function. P_{nm} is the Legendre polynomials. a_{nm} and s_{nm} are the expansion coefficients of incident velocity potential and scattering velocity potential, respectively. The boundary conditions of the general structure in the acoustic scattering process are continuous sound pressure and continuous normal velocity,

$$\begin{aligned} i\rho_e \omega \Phi_{in}(r, \theta, \omega) &= i\rho_0 \omega \Phi_{out}(r, \theta, \omega), \\ \frac{\partial \Phi}{\partial r}_{in} &= \frac{\partial \Phi}{\partial r}_{out}. \end{aligned} \quad (4)$$

Because the integral surface is arbitrarily selected, the integral radius can be large enough to satisfy the far-field condition. If $kr \rightarrow \infty$, the approximate expressions of the first kind of spherical Bessel function and Hankel function are written, respectively, as

$$\begin{aligned} j_n(kr) &= \frac{i^{-(n-1)} e^{ikr} + i^{n+1} e^{-ikr}}{2kr}, \\ h_n^{(1)}(kr) &= \frac{i^{-(n+1)} e^{ikr}}{kr}. \end{aligned} \quad (5)$$

So, the expression of ARF can be obtained from the above, which greatly simplifies the calculation,

$$\begin{aligned} \mathbf{F} &= \frac{1}{2} \rho_0 k^2 \iint_{S'} \text{Re} \left[- \sum_{nm} \sum_{n'm'} \frac{i^{n'-n}}{(kr)^2} (a_{nm} + s_{nm}) \right. \\ &\quad \left. * s_{n'm'}^* Y_{nm}(\theta, \phi) Y_{n'm'}^*(\theta, \phi) \right] \mathbf{n} dS, \\ \mathbf{F} &= \pi r_0^2 I_0 c_0^{-1} \mathbf{Y}, \\ I_0 &= \frac{(\rho_0 c_0)}{2} (k\Phi_0)^2. \end{aligned} \quad (6)$$

Here, \mathbf{Y} is the normalized acoustic radiation force. Since the structure scale interval of calculating the ARF is generally in the same order of magnitude as the wavelength, it is unnecessary to consider the acoustic scattering in Rayleigh region (the wavelength is larger than the structure scale) and optical region (the wavelength is smaller than the structure scale).

The case can be analyzed as follows: A spherical envelope is selected to minimize the computational complexity of the integration.

The density and compressibility coefficient of the studied structures (particles) are set as ρ_e and μ_e , and the compressibility coefficient of environmental media is set as μ_0 . If the time factor $e^{-i\omega t}$ is omitted, there is a general expression for the outgoing wave:

$$\psi_{\sigma mn}(k_0 r) = (\epsilon_m \gamma_{mn})^{1/2} h_n(k_0 r) Y_{\sigma mn}(\theta, \phi). \quad (7)$$

The value range of sum parameter m and n in Eq. (7) is $m = 0, 1, \dots, n$ and $n = 0, 1, \dots, \sigma = e/o$ is the parity mark of Hankel function $h_n(kr) = j_n(kr) + in_n(kr)$. ϵ_m is the Neumann factor. γ_{mn} is the undetermined parameter.

A refractive index is defined as $q = k_e/k_0$, where k_0 and k_e are the wave numbers in the environmental media and the studied structures. In order to reduce the complexity of representation of $\psi_{\sigma mn}$, we define a single parameter $\chi_{\sigma mn}$ to describe the impact of ρ_e/ρ_0 and k_e/k_0 on the results. For incident waves,

$$\chi_{\sigma mn}(k_0 r) = \frac{2q^n (\epsilon_m \gamma_{mn})^{1/2} j_n(k_0 r) Y_{\sigma mn}(\theta, \phi)}{(1 + \rho_0/\rho_e)}. \quad (8)$$

For transmitted waves,

$$\chi_{\sigma mn}(k_e r) = \frac{2q^{-n} (\epsilon_m \gamma_{mn})^{1/2} j_n(k_e r) Y_{\sigma mn}(\theta, \phi)}{(1 + \rho_e/\rho_0)}, \quad (9)$$

where $Y_{\sigma mn}(\theta, \phi)$ is the spherical harmonic function.

In order to express the one-to-one correspondence relationship here, ν is defined as the characteristic parameter instead of σ, m , and n . The studied region can be divided into three functions: incident, scattering, and transmission. For incident waves,

$$\Phi_i(k_0 r) = \sum_{\nu=1} a_{\nu} \chi_{\nu}(k_0 r). \quad (10)$$

For scattering waves and interior waves,

$$\begin{aligned} \Phi_s(k_0 r) &= \sum_{\nu=1} s_{\nu} \chi_{\nu}(k_0 r), \\ \Phi_{int}(k_0 r) &= \sum_{\nu=1} \alpha_{\nu} \chi_{\nu}(k_0 r). \end{aligned} \quad (11)$$

So the problem is transformed into the problem of solving s_{ν} with known a_{ν} . For a given incident wave parameter a_{ν} , the problem is transformed into the calculation of scattering wave parameter s_{ν} and internal wave parameter α_{ν} . Q matrix is defined to solve this problem,

$$Q_{uv} = \frac{k_0}{4\pi} \int d\sigma * [(\rho_e/\rho_0) \chi_u(k_e r) \nabla \Phi_v(k_0 r) - \nabla \chi_u(k_e r) \Phi_v(k_0 r)], \quad (12)$$

where σ is the panel of the structural surface. The relationship among the three coefficients in Eqs. (10) and (11) could be described by the Q matrix as follows:³⁹

$$\begin{aligned} iQ\alpha_{\nu} &= a_{\nu}, \\ s_{\nu} &= -i\text{Reg}(Q)\alpha_{\nu}. \end{aligned} \quad (13)$$

Reg is the regular wave function. By replacing the Hankel function with the Bessel function and the Neumann function, the Q matrix can be divided into regular matrix R and singular matrix S: $Q = R + iS$. The relationship between scattering parameters and incident parameters can be expressed by the definition of T matrix: $s_{\nu} = Ta_{\nu}$. Since the reciprocity principle is satisfied in the studied range (because the

reciprocity principle is only satisfied in the linear range, viscosity needs to be excluded), T matrix is the symmetric matrix,

$$T = -Q^{-1}R = -(R + iS)^{-1}R. \quad (14)$$

If the focus is on the sound field inside the structure, the inward propagation matrix G should be defined and calculated. Due to the mode conversion on the surface of the non-rigid medium, transverse waves will be generated. However, after the non-viscous medium environment forms a stable state, a stable standing wave field is formed inside the structure, and no radiation stress tensor dissipation will occur. Therefore, the surface mode conversion part for non-rigid media can be incorporated into matrix G. Since the goal is to calculate the ARF, not the acoustic radiation of the entire region, there is no need to pay specific attention to the standing wave structure inside or near the particle due to mode conversion. The calculation can be performed only by obtaining the sound pressure at any envelope surface that is convenient for calculation. According to the previous derivation, this particular envelope surface is generally selected in the far field. The inward propagation matrix is determined by the inward energy flow of the studied structure,

$$\begin{aligned} G &= \frac{1}{4} (Q^{-1})^{\dagger} (W + W^{\dagger}) Q^{-1}, \\ W_{\mu\nu} &= \frac{k_0}{4\pi} \int d\sigma * \frac{\rho}{\rho_0} \chi_{\mu}(k_e r) \nabla \chi_{\nu}(k_e r) \\ -\text{Re}(T) &= T^{\dagger}T + \frac{1}{4}G, \\ S^{\dagger}S &= I - G, \end{aligned} \quad (15)$$

where \dagger denotes conjugate transposition. A special example can be given to verify the correctness of the solution: if the total scattering is not transmitted, S is the unit matrix, then there will be an inward propagation matrix $G=0$.

Since the radius of envelope surface can be defined freely, we can make $kr \gg 1$, then $\psi_{sca}(kr)$ is proportional to $\zeta(\theta, \phi)e^{ikr}/ikr$. Here, the angle parameter function

$$\zeta(\theta, \phi) = - \sum_{\nu, \nu'=1}^N a_{\nu} T_{\nu\nu'} (-1)^{\nu'} Y_{\nu'}(\theta, \phi). \quad (16)$$

It can be noted that for particles with high symmetry, such as for particles rotating symmetrically along the beam propagation direction, the Q matrix can be decoupled,

$$Q_{\sigma mn \sigma' m' n'} = \delta_{\sigma' \sigma} \delta_{mm'} Q_{nn'}^{\sigma m}. \quad (17)$$

To simplify the form of representation of Q, we define

$$x(\theta) = kr(\theta). \quad (18)$$

Hence,

$$\begin{aligned} \sin \theta \frac{dP_n^m(\cos \theta)}{d\theta} &= (n-m+1)P_{n+1}^m(\cos \theta) \\ &\quad - (n+1) \cos \theta P_n^m(\cos \theta), \\ \frac{dj_n(x)}{dx} &= \frac{n}{x} j_n(x) - j_{n+1}(x), \\ \frac{dn_n(x)}{dx} &= \frac{n+1}{x} n_n(x) + n_{n-1}(x). \end{aligned} \quad (19)$$

Back into the matrix Q_{uv} , the following results can be deduced:

$$S_{nn'} = d_{nn'} \int_0^\pi d\theta \left\{ j_n(qx) n_{n'}(x) G_{nn'}(\theta) + \left[\frac{\rho_e}{\rho_0} j_n(qx) n_{n'-1}(x) + q j_{n+1}(qx) n_{n'-1}(x) \right] \right\} H_{nn'}(\theta). \quad (20)$$

For the sake of simplicity, the angle parameters that can be separated are taken out separately,

$$G_{nn'} = \left\{ \left[\frac{\rho_e}{\rho_0} (n' + 1) - (n + 1) \right] r'(\theta) \cos \theta - \left[\frac{\rho_e}{\rho_0} (n' + 1) + n \right] r(\theta) \sin \theta \right\} * P_n^m(\cos \theta) P_{n'}^m(\cos \theta) + r'(\theta) [(n - m + 1) P_{n+1}^m(\cos \theta) P_{n'}^m(\cos \theta) - \frac{\rho_e}{\rho_0} (n' - m + 1) P_n^m(\cos \theta) P_{n'+1}^m(\cos \theta)], \quad (21)$$

$$H_{nn'}(\theta) = r^2(\theta) \sin \theta P_n^m(\cos \theta) P_{n'}^m(\cos \theta). \quad (22)$$

The normalization parameter can be defined as follows:

$$d_{nn'} = 2 \left(1 + \frac{\rho}{\rho_0} \right)^{-1} q^{-n} (\gamma_{mn} \gamma_{mn'})^{\frac{1}{2}}. \quad (23)$$

The matrix R can be obtained by replacing $n_s(x)$ with $j_s(x)$. To sum up, the analytical solution for the case that the three dimensions and wavelengths are in the same order of magnitude is deduced. By calculating the R matrix and S matrix, the Q matrix is obtained. Through the calculation of s_v , the velocity potential of the scattering field is obtained. Hence, the ARF is finally obtained.

III. NUMERICAL SIMULATION AND FINITE ELEMENT SIMULATION VERIFICATION

In order to verify the correctness of the proposed scheme, finite element simulation and numerical simulation based on the method proposed in the scheme are used for comparison. Since all beams can be decomposed into plane wave combinations by means of spectrum analysis, in order to illustrate the correctness of the proposed scheme, sweep of plane waves can be used in the simulation. Several basic particles and composite structures are selected for verification, including spherical particles, ellipsoid particles, cylindrical particles, spherical annular particles, and combination of spherical particles. For possible future medical applications, the samples are in millimeter level. In this work, finite element simulations are implemented using the software COMSOL 6.1. The maximum cell size for meshing is 1/6 of the wavelength. The maximum cell growth rate is 1.5. The curvature factor is 0.6. Narrow area resolution is 0.5. In boundary handling, iterations for smooth transition are added to internal meshes. The number of iterations is four. The division method of the surface mesh is quadrilateral, and the number of iterations in the sweeping process in the modeling is four times. Sharp edges are handled by splitting. The minimum angle that is split during the splitting process is 240° , and the maximum angle obtained by splitting is 100° . In the simulation, the environmental medium is water. The structural material is aluminum. The relevant parameters of the simulation are shown in Table I.

In this numerical simulation, the parameters are set as follows:

1. The radius of spherical particles varies from 0.0010 to 0.0015 m [shown in Fig. 2(a)].

TABLE I. Parameter selection of finite element simulation.

Parameter	Symbols	Numerical value
Incident wave frequency	f_0	250 kHz
Sound velocity of medium	c_0	1500 m/s
Density of medium	ρ_0	1000 kg/m ³
Density of structure	ρ_e	2700 kg/m ³
Young's modulus of structure	E_e	70 GPa
Poisson's ratio of structure	ν_e	0.33

2. The length of the two minor axes of the ellipsoid particle varies from 0.0010 to 0.0015 m. The length of the major axis is 1.5 times of the minor axis [shown in Fig. 2(b)].
3. The cross section radius of cylindrical particles varies from 0.0010 to 0.0015 m. The height of cylindrical particles is the same as the cross section radius [shown in Fig. 2(c)].
4. The inner diameter of the spherical ring varies from 0.0010 to 0.0015 m. The outer diameter of the spherical ring is twice that of the inner diameter [shown in Fig. 2(d)].
5. In the combination of spherical particles, the radius of each sphere varies from 0.0010 to 0.0015 m. There is no spacing between individual particles [shown in Fig. 2(e)].
6. In the array of spherical particles, the radius of each sphere varies from 0.0005 to 0.00075 m. There is no spacing between individual particles [shown in Fig. 2(f)].

The shapes of the selected structures are shown in the schematic Fig. 2. The comparison between the results obtained by using the finite element simulation and the numerical simulation based on the method proposed is shown in Figs. 3–20. The scan images obtained by the finite element simulation are shown in Figs. 3, 6, 9, 12, 15, and 18, which are considered to be accurate results. In contrast, numerical scan images based on the proposed method is shown in Figs. 4, 7, 10, 13, 16, and 19. The abscissa of the figure is the corresponding scale parameter. The ordinate of the figure is the frequency of the incident plane wave. To better illustrate the correctness of the proposed method, a comparative 3D image is drawn, as shown in Figs. 5, 8, 11,

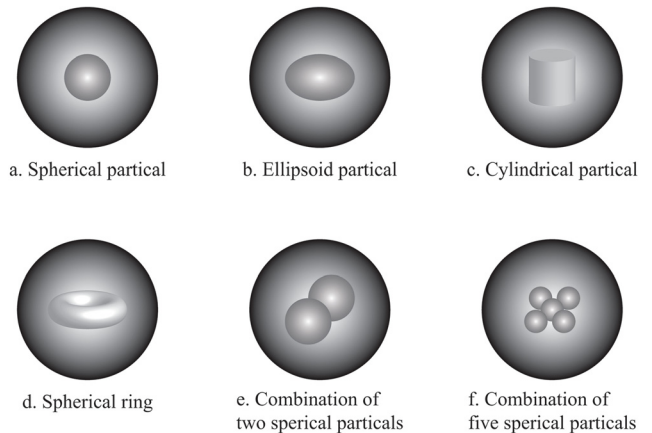


FIG. 2. Shapes of simulated structures and the envelope surface.

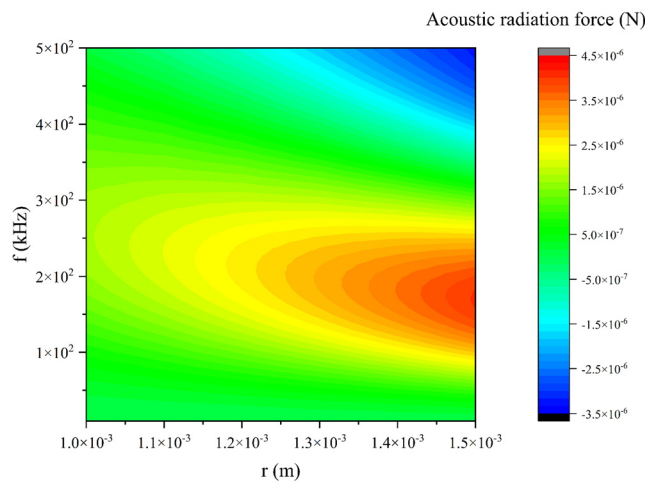


FIG. 3. ARFs on a spherical particle calculated by finite element simulation. The radius of spherical particles varies from 0.0010 to 0.0015 m. Incident frequency varies from 10 to 500 kHz.

14, 17, and 20. The height coordinate of the 3D image represents the value of ARF. The points in the figure are the results obtained by the finite element simulation. The error bars represent the difference between the analytical solution of the proposed calculation scheme and the results obtained from the finite element simulation. The simulation of several structures can be seen from Figs. 3–20, and the results obtained by the two methods are basically consistent within the allowable error range. The difference between the finite element simulation and the proposed analytical method is mainly due to truncation error. This further verifies the correctness of the proposed analytical solution.

In previous processing methods, unless the structure has good symmetry, the ARF of complex structures can only be obtained by

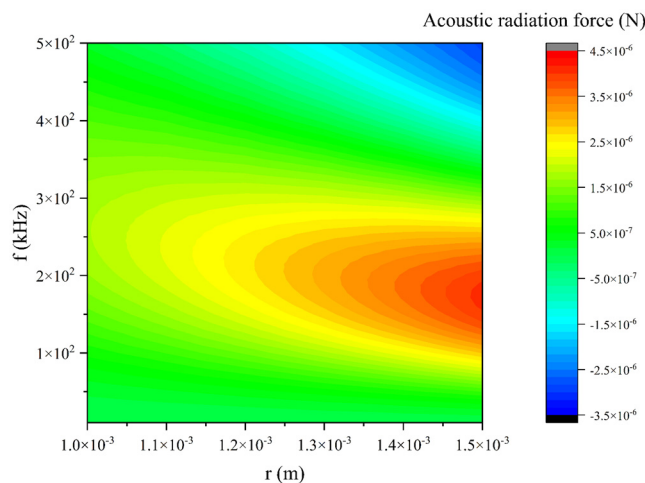


FIG. 4. ARFs on a spherical particle calculated by the proposed theoretical solution. The radius of spherical particles varies from 0.0010 to 0.0015 m. Incident frequency varies from 10 to 500 kHz.

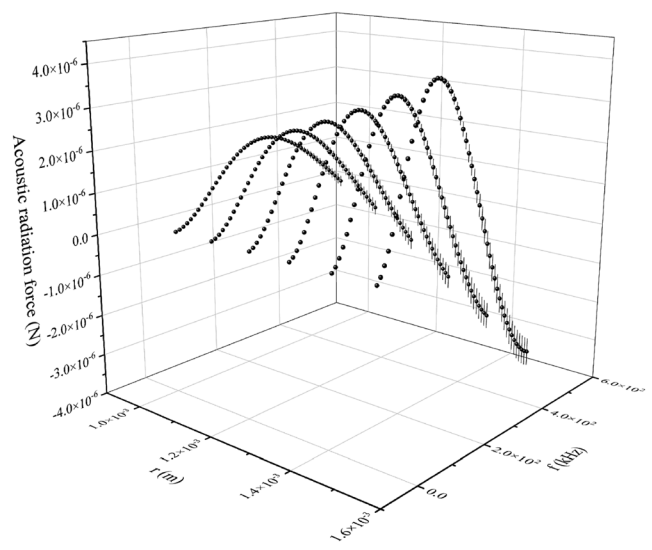


FIG. 5. Comparison of ARFs on a spherical particle calculated by finite element simulation and the proposed theoretical solution. The radius of spherical particles varies from 0.0010 to 0.0015 m. Incident frequency varies from 10 to 500 kHz. The points are the results obtained by finite element simulation. The error bars represent the difference between the analytical solution of the proposed calculation scheme and the results obtained from the finite element simulation.

finite element simulation. For example, in the two examples of Figs. 2(d) and 2(f), due to the existence of multiple scattering, the traditional definition method can hardly calculate the ARF of the spherical ring particle and combination of multiple spherical particles. However, based on the method proposed in this work, only the transfer matrix of the scattered radiation stress tensor should be paid attention to during the calculation of the ARF, and the internal structural information is not required, which greatly simplifies the calculation process of the ARF.

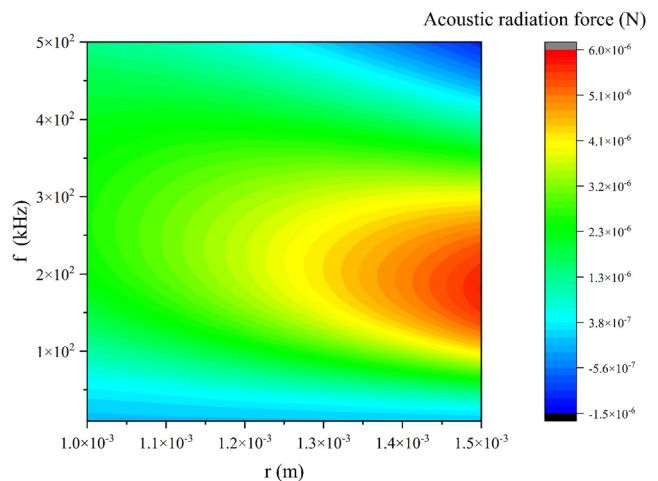


FIG. 6. ARFs on an ellipsoid particle calculated by finite element simulation. The length of the two minor axis of the ellipsoid particle varies from 0.0010 to 0.0015 m. The length of the major axis is 1.5 times of the minor axis. Incident frequency varies from 10 to 500 kHz.

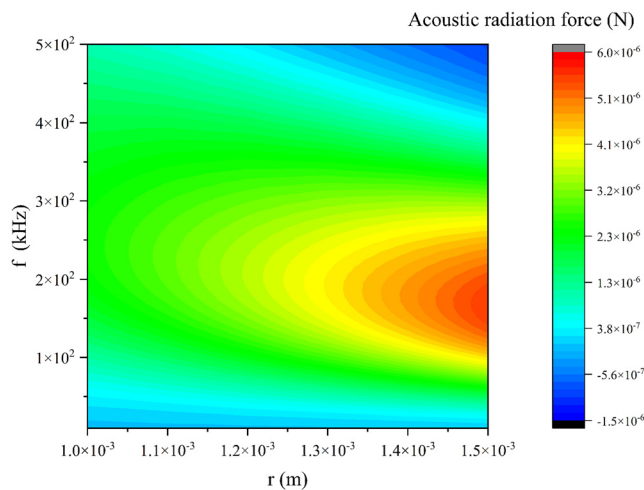


FIG. 7. ARFs on an ellipsoid particle calculated by the proposed theoretical solution. The length of the two minor axis of the ellipsoid particle varies from 0.0010 to 0.0015 m. The length of the major axis is 1.5 times of the minor axis. Incident frequency varies from 10 to 500 kHz.

From the comparison of theoretical calculation results and finite element simulation in the case of Figs. 3–20, it can be seen that the ARF on the complex structure can be handled, and the errors of each case are within an acceptable range. Figures 12–14 and 18–20 also verify the processing ability of our method to calculate the ARF of the spherical ring particle and combination of multiple spherical particles, which is also the

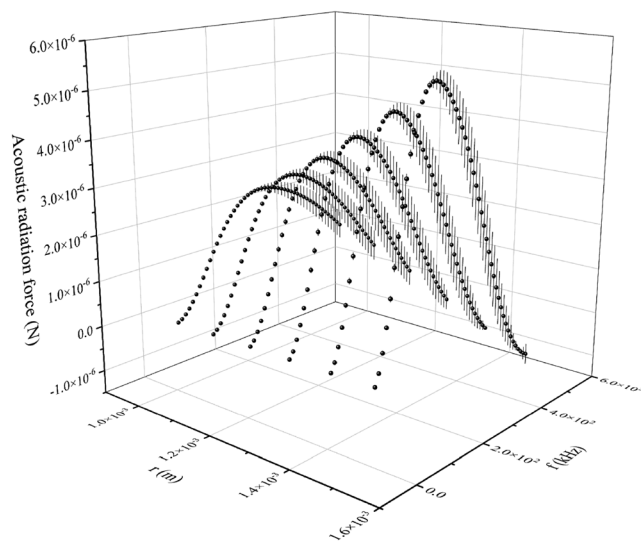


FIG. 8. Comparison of ARFs on an ellipsoid particle calculated by finite element simulation and the proposed theoretical solution. The length of the two minor axis of the ellipsoid particle varies from 0.0010 to 0.0015 m. The length of the major axis is 1.5 times of the minor axis. Incident frequency varies from 10 to 500 kHz. The points are the results obtained by finite element simulation. The error bars represent the difference between the analytical solution of the proposed calculation scheme and the results obtained from the finite element simulation.

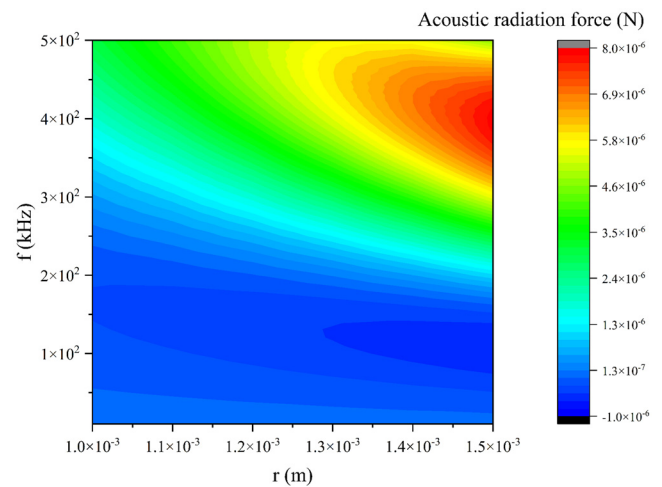


FIG. 9. ARFs on a cylindrical particle calculated by finite element simulation. The cross section radius of cylindrical particles varies from 0.0010 to 0.0015 m. The height of cylindrical particles is the same as the cross section radius. Incident frequency varies from 10 to 500 kHz.

analytical method for calculating the ARF of these two structures proposed for the first time.

In the cases of the spherical ring, the combination of spherical particles, and the array of spherical particles, the error increased compared to other cases. This is due to the slow convergence of the series in the transfer matrix in these few cases compared to the transfer matrix from the controlled structure to the computed envelope surface in the other cases. In order to unify the calculation method, we used the same number of truncation terms, which resulted in slightly larger truncation errors in the calculation process of these cases. Increasing the calculation terms of the series can effectively reduce this error.

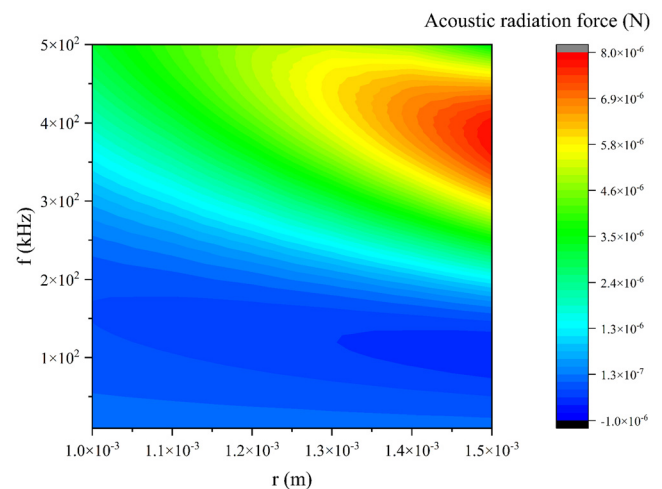


FIG. 10. ARFs on a cylindrical particle calculated by the proposed theoretical solution. The cross section radius of cylindrical particles varies from 0.0010 to 0.0015 m. The height of cylindrical particles is the same as the cross section radius. Incident frequency varies from 10 to 500 kHz.

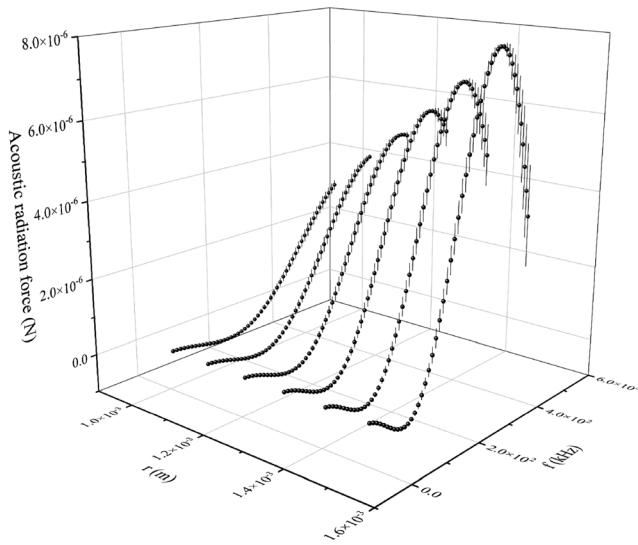


FIG. 11. Comparison of ARFs on a cylindrical particle calculated by finite element simulation and the proposed theoretical solution. The cross section radius of cylindrical particles varies from 0.0010 to 0.0015 m. The height of cylindrical particles is the same as the cross section radius. Incident frequency varies from 10 to 500 kHz. The points are the results obtained by finite element simulation. The error bars represent the difference between the analytical solution of the proposed calculation scheme and the results obtained from the finite element simulation.

In practical applications, the surface shape of particles is mostly irregular, which is difficult to describe with accurate mathematical expression. Therefore, the calculation complexity can be greatly reduced by using the self-defined peripheral envelope to avoid the integration process on the particle surface. For systems with multiple particles, such as periodic particle arrays, it is usually quite difficult to

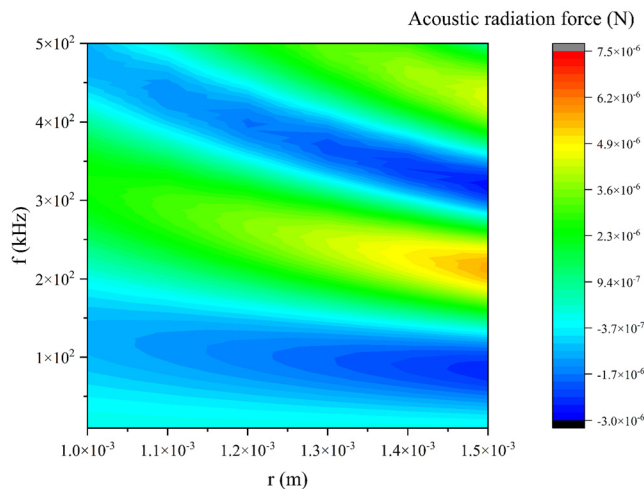


FIG. 12. ARFs on a spherical ring particle calculated by finite element simulation. The inner diameter of the spherical ring varies from 0.0010 to 0.0015 m. The outer diameter of the spherical ring is twice that of the inner diameter. Incident frequency varies from 10 to 500 kHz.

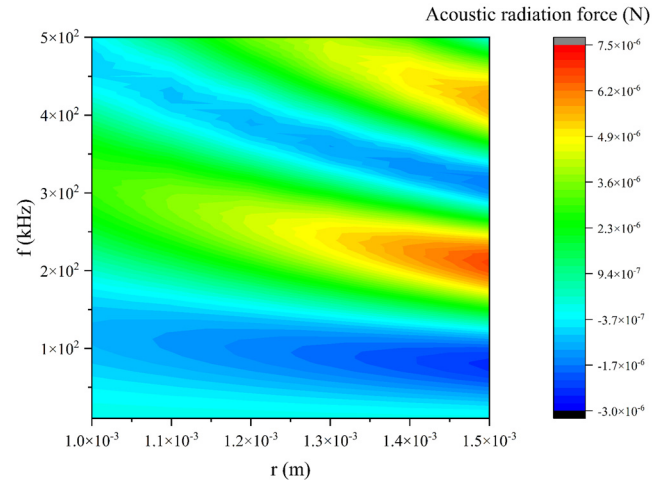


FIG. 13. ARFs on a spherical ring particle calculated by the proposed theoretical solution. The inner diameter of the spherical ring varies from 0.0010 to 0.0015 m. The outer diameter of the spherical ring is twice that of the inner diameter. Incident frequency varies from 10 to 500 kHz.

obtain the ARF they received. However, with integral extension, the problem becomes manageable.

IV. DISCUSSIONS AND CONCLUSIONS

An analytical scheme of ARF acting on general uniform structure is deduced. The correctness and accuracy of the algorithm are verified by comparison with finite element simulation. In the derivation

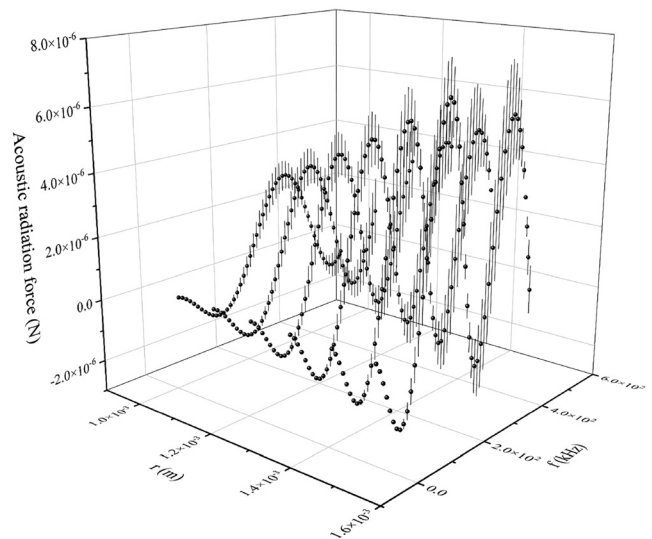


FIG. 14. Comparison of ARFs on a spherical ring particle calculated by finite element simulation and the proposed theoretical solution. The inner diameter of the spherical ring varies from 0.0010 to 0.0015 m. The outer diameter of the spherical ring is twice that of the inner diameter. Incident frequency varies from 10 to 500 kHz. The points are the results obtained by finite element simulation. The error bars represent the difference between the analytical solution of the proposed calculation scheme and the results obtained from the finite element simulation.

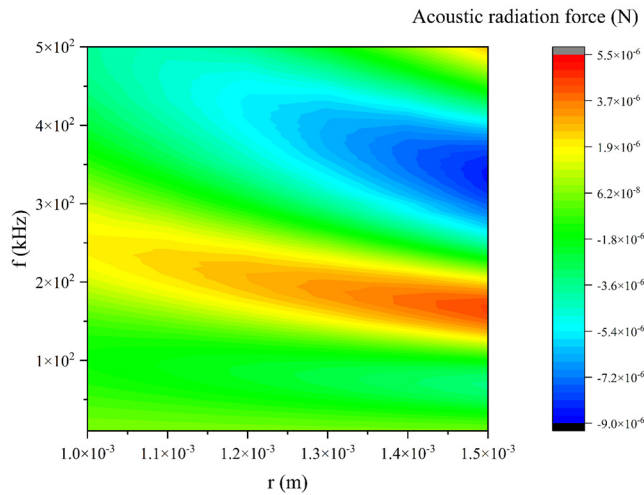


FIG. 15. ARFs on combination of two spherical particles calculated by finite element simulation. The radius of each sphere varies from 0.0010 to 0.0015 m. Incident frequency varies from 10 to 500 kHz.

process, the original transmission matrix for rigid particles has been extended to the non-rigid case.

In the process of performing theoretical calculations, limitations arise from the computational capabilities of the computer. In this work, the integration process is achieved through summation, and the differentiation process is implemented through finite differences. When performing calculations, infinite series summations are typically truncated after the first five terms, with a larger number of terms taken for slowly converging series. Throughout these processes, truncation errors and rounding errors are introduced. If we have abundant computational resources, we can obtain more accurate predictive results by

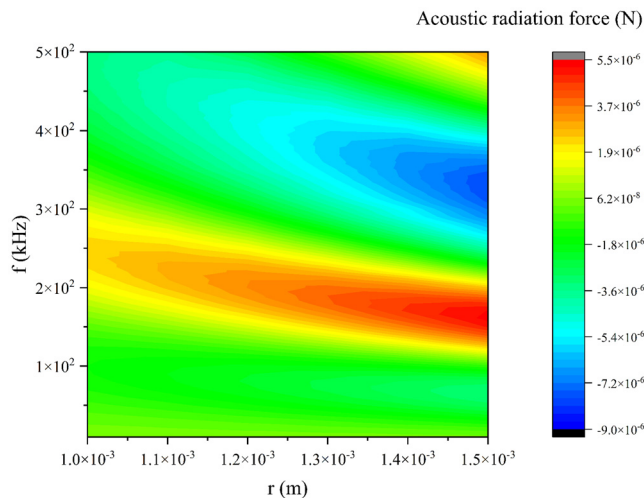


FIG. 16. ARFs on combination of two spherical particles calculated by the proposed theoretical solution. The radius of each sphere varies from 0.0010 to 0.0015 m. Incident frequency varies from 10 kHz to 500 kHz. Incident frequency varies from 10 to 500 kHz.

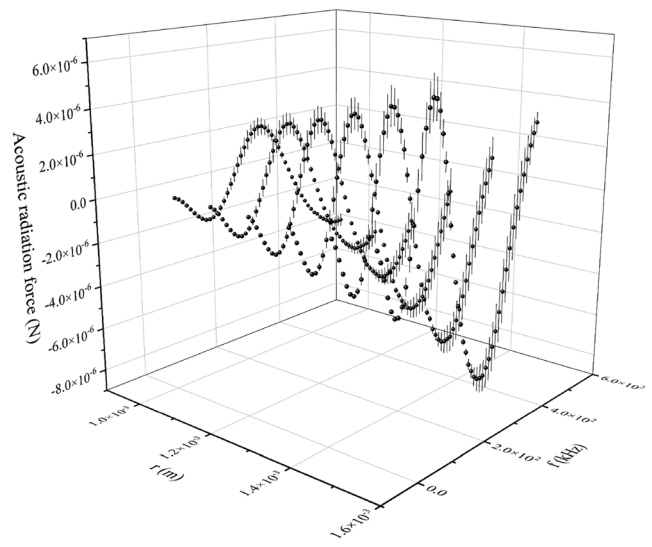


FIG. 17. Comparison of ARFs on combination of two spherical particles calculated by finite element simulation and the proposed theoretical solution. The radius of each sphere varies from 0.0010 to 0.0015 m. Incident frequency varies from 10 to 500 kHz. The points are the results obtained by finite element simulation. The error bars represent the difference between the analytical solution of the proposed calculation scheme and the results obtained from the finite element simulation.

increasing the computational precision, such as reducing the discretization step size and increasing the number of terms in the series calculations.

Compared with the method of numerical simulation to obtain the ARF, it is of great significance to obtain the analytical solution of the ARF of the general structure for regulating the ARF. This method effectively avoids the integration of complex particle surfaces, which only needs to calculate the scattering velocity potential on the specified

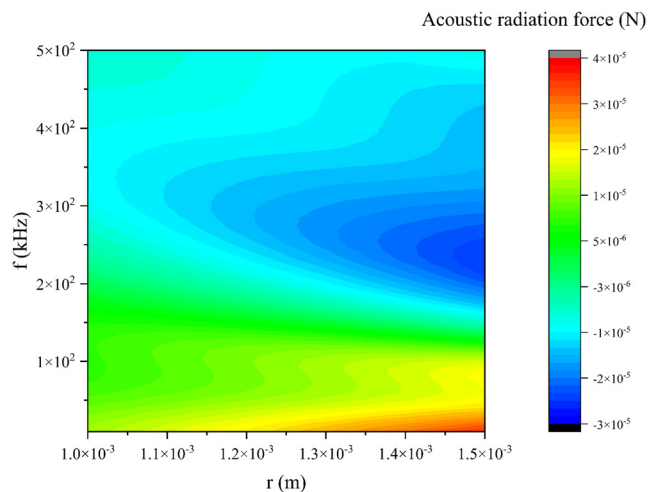


FIG. 18. ARFs on combination of five spherical particles calculated by finite element simulation. The radius of each sphere varies from 0.0010 to 0.0015 m. Incident frequency varies from 10 to 500 kHz.

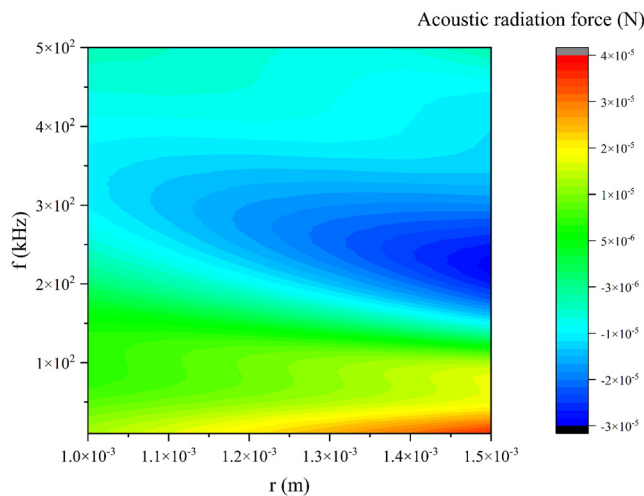


FIG. 19. ARFs on combination of five spherical particles calculated by the proposed theoretical solution. The radius of each sphere varies from 0.0010 to 0.0015 m. Incident frequency varies from 10 to 500 kHz.

envelope surface. This simplification is of great significance in the real-time calculation of ARF, which has important application prospects in structure and particle manipulation, medicine, and materials science, which also makes it possible to use ARF upon large-scale structure and particle to realize accurate and real-time manipulation applications. It makes it possible to solve the analytical solution of the ARF on complex structures, which can only be obtained by finite element simulation in most cases. Based on the analysis, the ARF received by the

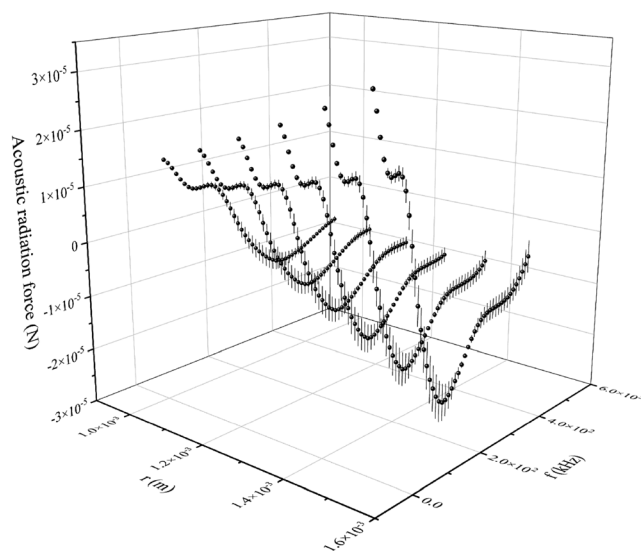


FIG. 20. Comparison of ARFs on combination of five spherical particles calculated by finite element simulation and the proposed theoretical solution. The radius of each sphere varies from 0.0010 to 0.0015 m. Incident frequency varies from 10 to 500 kHz. The points are the results obtained by finite element simulation. The error bars represent the difference between the analytical solution of the proposed calculation scheme and the results obtained from the finite element simulation.

array structure also becomes easy to handle. As crystals composed of periodic structures have become a recent hot spot, accurate manipulation of crystals also can be achieved. Based on the proposed scheme, it is possible to assign the momentum of particles and structures by ARF, which provides a new and effective method for structure manipulation and control in fluid.

ACKNOWLEDGMENTS

This project was supported by the National Key R&D Program of China (No. 2020YFA0211400), the State Key Program of the National Natural Science of China (No. 11834008), the National Natural Science Foundation of China (Nos. 12174192 and 12204119), the State Key Laboratory of Acoustics, Chinese Academy of Sciences (No. SKLA202210), the Key Laboratory of Underwater Acoustic Environment, Chinese Academy of Sciences (No. SSHJ-KFKT-1701), and the Guizhou Provincial Science and Technology Foundation (No. ZK[2023]249).

AUTHOR DECLARATIONS

Conflict of Interest

The authors have no conflicts to disclose.

Author Contributions

Menyang Gong and Yupei Qiao contributed equally to this work.

Menyang Gong: Conceptualization (lead); Data curation (lead); Formal analysis (lead); Investigation (lead); Methodology (lead); Project administration (lead); Software (equal); Supervision (lead); Validation (lead); Visualization (lead); Writing – original draft (lead); Writing – review & editing (equal). **Yupei Qiao:** Software (equal). **Xin Xu:** Visualization (supporting). **Jiehui Liu:** Methodology (supporting). **Aijun He:** Methodology (supporting). **Xiaozhou Liu:** Funding acquisition (lead); Project administration (supporting); Resources (lead); Writing – review & editing (equal).

DATA AVAILABILITY

The data that support the findings of this study are available from the corresponding author upon reasonable request.

REFERENCES

- A. Ashkin, "Forces of a single-beam gradient laser trap on a dielectric sphere in the ray optics regime," *Biophys. J.* **61**, 569–582 (1992).
- J. R. Wu, "Acoustical tweezers," *J. Acoust. Soc. Am.* **89**, 2140–2143 (1991).
- T. Hasegawa, M. Ochi, and K. Matsuzawa, "Acoustic radiation force on a solid elastic sphere in a spherical wave field," *J. Acoust. Soc. Am.* **69**, 937–942 (1981).
- T. Hasegawa and K. Yosioka, "Acoustic radiation force on fused silica spheres, and intensity determination," *J. Acoust. Soc. Am.* **58**, 581–585 (1975).
- W. L. Nyborg, "Radiation pressure on a small rigid sphere," *J. Acoust. Soc. Am.* **42**, 947 (1967).
- P. J. Westervelt, "Acoustic radiation pressure," *J. Acoust. Soc. Am.* **29**, 26–29 (1957).
- J. R. Wu and G. H. Du, "Acoustic radiation force on a small compressible sphere in a focused beam," *J. Acoust. Soc. Am.* **87**, 997–1003 (1990).
- X. F. Zhang and G. B. Zhang, "Acoustic radiation force of a gaussian beam incident on spherical particles in water," *Ultrasound Med. Biol.* **38**, 2007–2017 (2012).

- ⁹M. Azarpeyvand, "Acoustic radiation force of a Bessel beam on a porous sphere," *J. Acoust. Soc. Am.* **131**, 4337–4348 (2012).
- ¹⁰M. Azarpeyvand, "Prediction of negative radiation forces due to a Bessel beam," *J. Acoust. Soc. Am.* **136**, 547–555 (2014).
- ¹¹D. Baresch, J. L. Thomas, and R. Marchiano, "Three-dimensional acoustic radiation force on an arbitrarily located elastic sphere," *J. Acoust. Soc. Am.* **133**, 25–36 (2013).
- ¹²D. Baresch, J. L. Thomas, and R. Marchiano, "Observation of a single-beam gradient force acoustical trap for elastic particles: Acoustical tweezers," *Phys. Rev. Lett.* **116**, 024301 (2016).
- ¹³X. D. Fan and L. K. Zhang, "Trapping force of acoustical Bessel beams on a sphere and stable tractor beams," *Phys. Rev. Appl.* **11**, 014055 (2019).
- ¹⁴Z. X. Gong, P. L. Marston, W. Li, and Y. B. Chai, "Multipole expansion of acoustical Bessel beams with arbitrary order and location," *J. Acoust. Soc. Am.* **141**, El574–El578 (2017).
- ¹⁵W. Li and M. S. Wang, "Scattering of an arbitrary order acoustical Bessel beam by a rigid off-axis spheroid," *J. Acoust. Soc. Am.* **143**, 3676–3687 (2018).
- ¹⁶P. L. Marston, "Axial radiation force of a Bessel beam on a sphere and direction reversal of the force," *J. Acoust. Soc. Am.* **120**, 3518–3524 (2006).
- ¹⁷P. L. Marston, "Negative axial radiation forces on solid spheres and shells in a Bessel beam (I)," *J. Acoust. Soc. Am.* **122**, 3162–3165 (2007).
- ¹⁸P. L. Marston, "Radiation force of a helicoidal Bessel beam on a sphere," *J. Acoust. Soc. Am.* **125**, 3539–3547 (2009).
- ¹⁹Y. P. Qiao, J. Y. Shi, X. F. Zhang, and G. B. Zhang, "Acoustic radiation force on a rigid cylinder in an off-axis gaussian beam near an impedance boundary," *Wave Motion* **83**, 111–120 (2018).
- ²⁰Y. P. Qiao, X. F. Zhang, and G. B. Zhang, "Acoustic radiation force on a fluid cylindrical particle immersed in water near an impedance boundary," *J. Acoust. Soc. Am.* **141**, 4633–4641 (2017).
- ²¹O. A. Sapozhnikov and M. R. Bailey, "Radiation force of an arbitrary acoustic beam on an elastic sphere in a fluid," *J. Acoust. Soc. Am.* **133**, 661–676 (2013).
- ²²H. B. Wang, S. Gao, Y. P. Qiao, J. H. Liu, and X. Z. Liu, "Theoretical study of acoustic radiation force and torque on a pair of polymer cylindrical particles in two airy beams fields," *Phys. Fluids* **31**, 047103 (2019).
- ²³R. R. Wu, K. X. Cheng, X. Z. Liu, J. H. Liu, X. F. Gong, and Y. F. Li, "Study of axial acoustic radiation force on a sphere in a gaussian quasi-standing field," *Wave Motion* **62**, 63–74 (2016).
- ²⁴R. R. Wu, K. X. Cheng, X. Z. Liu, J. H. Liu, Y. W. Mao, and X. F. Gong, "Acoustic radiation force on a double-layer microsphere by a gaussian focused beam," *J. Appl. Phys.* **116**, 144903 (2014).
- ²⁵R. R. Wu, X. Z. Liu, and X. F. Gong, "Axial acoustic radiation force on a sphere in gaussian field," *AIP Conf. Proc.* **1685**, 040010 (2015).
- ²⁶L. K. Zhang, "A general theory of arbitrary Bessel beam scattering and interactions with a sphere," *J. Acoust. Soc. Am.* **143**, 2796–2800 (2018).
- ²⁷L. K. Zhang and P. L. Marston, "Geometrical interpretation of negative radiation forces of acoustical Bessel beams on spheres," *Phys. Rev. E* **84**, 035601 (2011).
- ²⁸L. K. Zhang and P. L. Marston, "Axial radiation force exerted by general non-diffracting beams," *J. Acoust. Soc. Am.* **131**, El329–El335 (2012).
- ²⁹S. Z. Hoque and A. K. Sen, "Interparticle acoustic radiation force between a pair of spherical particles in a liquid exposed to a standing bulk acoustic wave," *Phys. Fluids* **32**, 072004 (2020).
- ³⁰F. G. Mitri, "Radiation forces and torque on a rigid elliptical cylinder in acoustical plane progressive and (quasi) standing waves with arbitrary incidence," *Phys. Fluids* **28**, 077104 (2016).
- ³¹P. L. Marston, "Comment on 'Radiation forces and torque on a rigid elliptical cylinder in acoustical plane progressive and (quasi) standing waves with arbitrary incidence' [Phys. Fluids **28**, 077104 (2016)]," *Phys. Fluids* **29**, 029101 (2017).
- ³²M. Y. Gong, X. Xu, Y. P. Qiao, Z. H. Fei, Y. Y. Li, J. H. Liu, A. J. He, and X. Z. Liu, "Scheme of non-contact manipulation: Acoustic radiation force on spherical particle in a spherical shell structure," *Res. Phys.* **46**, 106264 (2023).
- ³³M. Y. Gong, X. Xu, Z. H. Fei, Y. Y. Li, T. Liu, S. L. Gao, J. H. Liu, A. J. He, and X. Z. Liu, "Non-invasive manipulation scheme of spherical particle in viscous fluids in a tube based on acoustic radiation force," *J. Acoust. Soc. Am.* **153**, 812–820 (2023).
- ³⁴M. Y. Gong, Y. P. Qiao, J. Lan, and X. Z. Liu, "Far-field particle manipulation scheme based on X wave," *Phys. Fluids* **32**, 117104 (2020).
- ³⁵M. Y. Gong, Y. P. Qiao, Z. H. Fei, Y. Y. Li, J. H. Liu, Y. W. Mao, A. J. He, and X. Z. Liu, "Non-diffractive acoustic beams produce negative radiation force in certain regions," *AIP Adv.* **11**, 065029 (2021).
- ³⁶G. Silva and F. Mitri, "Attraction by sound-examples on the negative acoustic radiation forces of Bessel 'tractor' beams on a sphere," *J. Acoust. Soc. Am.* **131**, 3534–3534 (2012).
- ³⁷Z. X. Gong and M. Baudoin, "Equivalence between angular spectrum-based and multipole expansion-based formulas of the acoustic radiation force and torque," *J. Acoust. Soc. Am.* **149**, 3469–3482 (2021).
- ³⁸Z. X. Gong, P. L. Marston, and W. Li, "T-matrix evaluation of three-dimensional acoustic radiation forces on nonspherical objects in Bessel beams with arbitrary order and location," *Phys. Rev. E* **99**, 063004 (2019).
- ³⁹P. C. Waterman, "Surface fields and the t matrix," *J. Opt. Soc. Am. A* **16**, 2968–2977 (1999).